



Controlled assemble of hollow heterostructured $g\text{-C}_3\text{N}_4@\text{CeO}_2$ with rich oxygen vacancies for enhanced photocatalytic CO_2 reduction

Mengfang Liang, Timur Borjigin, Yuhao Zhang, Beihong Liu, Hui Liu, Hong Guo*

School of Materials Science and Engineering, Yunnan University, No. 2, Green Lake North Road, Kunming 650091, China



ARTICLE INFO

Keywords:
 CO_2 reduction
 Oxygen vacancy
 Hollow heterostructures
 $g\text{-C}_3\text{N}_4@\text{CeO}_2$
 Visible light photocatalyst

ABSTRACT

Hollow heterostructured $g\text{-C}_3\text{N}_4@\text{CeO}_2$ photocatalysts with rich oxygen vacancies are controllable designed by a facile strategy. The synergistic effect and oxygen vacancies of $g\text{-C}_3\text{N}_4@\text{CeO}_2$ play the major role in the process of CO_2 reduction, leading to CH_4 generating much earlier and higher concentration than that of the pristine $g\text{-C}_3\text{N}_4$ and CeO_2 alone. Meanwhile, the unique hollow structures can make multiple reflections of light in the cavity, and thus enhance the utilization efficiency of light. Moreover, the L-cysteine offers amine groups and meanwhile is anchored on the surface of $g\text{-C}_3\text{N}_4$ during the synthesis process, and thus contributes greatly to the enhanced CO_2 adsorption capability. Additionally, the large CO_2 adsorption capability is also beneficial for the enhanced photocatalytic activity. Therefore, the novel photocatalysts exhibit a remarkable reduction performance for CO_2 reduction under visible light irradiation. The $g\text{-C}_3\text{N}_4@\text{CeO}_2$ (CeO_2 49.7 wt %) shows the highest yields of CH_4 ($3.5 \mu\text{mol g}^{-1}$), CH_3OH ($5.2 \mu\text{mol g}^{-1}$) and CO ($16.8 \mu\text{mol g}^{-1}$), which are higher than most of other latest reported $g\text{-C}_3\text{N}_4$ based photocatalysts for CO_2 photoreduction, including coupled with semiconductors and noble metal cocatalysts. This strategy might represent a novel way for the effective conversion of CO_2 to clean fuels and can also be great potential used in the energy and environmental science.

1. Introduction

With the increasing global energy demands and diminishing petroleum reserves, the conversion of solar to chemical energy by photocatalytic CO_2 reduction to CH_3OH , CH_4 and CO is one of the most promising strategy for the generation of clean fuels [1–4]. The conversion efficiency of CO_2 and utilization of solar energy are mainly determined by the photocatalyst, which is a core component of this technique. With this in mind, developing stable, high efficient, and low-cost photocatalyst, especially for the visible-light application, is of significance to bring the technique to the market. Among tremendous photocatalysts, the layered graphitic carbon nitride ($g\text{-C}_3\text{N}_4$) has been reported to show outstanding photocatalytic activity due to its high reducibility and visible-photoabsorption [5–11]. Meanwhile, $g\text{-C}_3\text{N}_4$ as a metal-free photocatalyst can be fabricated under mild conditions, resulting in a low cost. Despite its towering merits in catalytic activity and cost, the low surface area and rapid charge recombination existing in pristine $g\text{-C}_3\text{N}_4$ should be improved to promote its practical application with enhanced photocatalytic performance.

To solve aforementioned issues, combination of $g\text{-C}_3\text{N}_4$ with heterojunction semiconductors [5,6] has been proved to be an effective strategy to further improve the photocatalytic performance. In a deep

understanding, the closely contacted interface and well matched band structures between the heterojunction semiconductors and $g\text{-C}_3\text{N}_4$ can promote the separation of electron-hole and suppress charge recombination. Meanwhile, the electrons on $g\text{-C}_3\text{N}_4$ and holes on the heterojunction semiconductors present enhanced reducibility and oxidability. However, in spite of the higher charge separation efficiency, the transferred photoinduced carriers exhibited lower oxidation and reduction abilities than original electrons and holes in this way. Besides the coupled semiconductors, appropriate design of the nano-scale architectures can also improve their photocatalytic activity obviously. Among several nanostructures, hollow materials showed excellent photocatalytic performances due to their high specific surface areas and more available activity surfaces [12–15]. For example, our previously reported hollow structured TiO_2 and CeO_2 exhibit improved photocatalytic performance compared with their solid counterparts [16–18]. Furthermore, it is noticed that photocatalysts with rich oxygen vacancies exhibit enhanced charge separation efficiencies and undiminished photooxidation or photoreduction performances under visible light. For example, CeO_2 photocatalysts with rich oxygen vacancies have been proved to display superior photocatalytic activity used in energy and environmental fields [19–22]. Although these procedures are effective, each single strategy alone can provide only

* Corresponding author.

E-mail address: guohongcom@126.com (H. Guo).

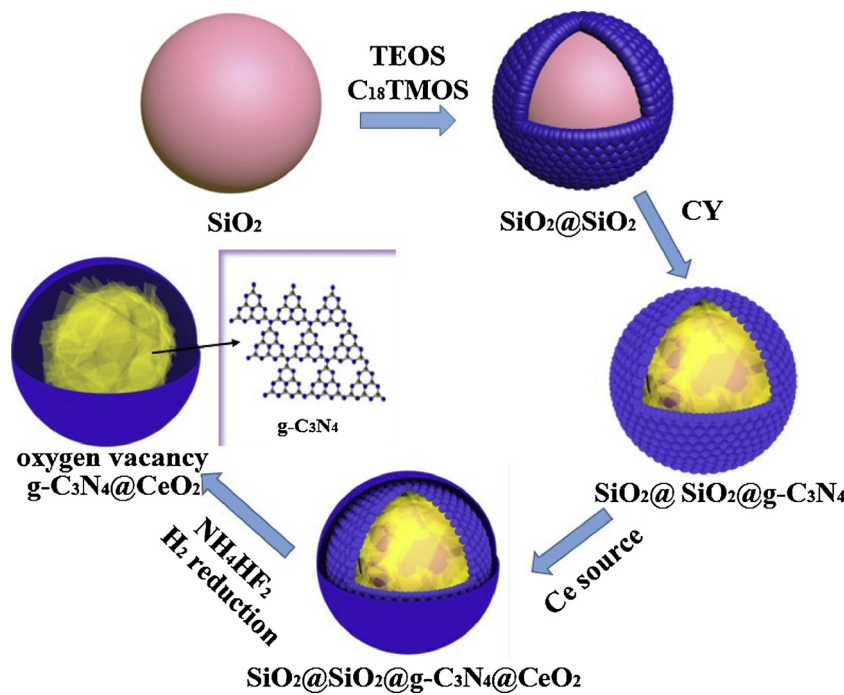


Fig. 1. Representative illustration of the assembling of $\text{g-C}_3\text{N}_4\text{@CeO}_2$ hollow heterostructures.

limited improvement in the photocatalytic activity for the reduction of CO_2 . Therefore, development of a controllable fabrication of hollow $\text{g-C}_3\text{N}_4$ -based photocatalysts coupled with rich oxygen vacancies used for enhanced photocatalytic CO_2 reduction is still highly desired.

CeO_2 with rich oxygen vacancies has received much attention on photocatalysis technology due to its intriguing optical and electrical performance [20–24], and it can also form heterojunctions with $\text{g-C}_3\text{N}_4$ due to their matched band potentials. However, to the best of our knowledge, there are no reports on hollow $\text{g-C}_3\text{N}_4\text{@CeO}_2$ with rich oxygen vacancies used as photocatalytic performance for the CO_2 reduction previously. Herein, combining the virtues of heterostructures, rich oxygen vacancies and hollow structure, we designed hollow structured $\text{g-C}_3\text{N}_4\text{@CeO}_2$ with rich oxygen vacancies, possessing excellent visible-light photocatalyst activity to reduce CO_2 as illustrated in Fig. 1. The SiO_2 was prepared first and then used as the template to fabricate uniform core-shell $\text{g-C}_3\text{N}_4$ nanospheres. Subsequently, coupling CeO_2 gave the desired $\text{g-C}_3\text{N}_4\text{@CeO}_2$ after NH_4HF_2 washing and heat treatment. Finally, hollow $\text{g-C}_3\text{N}_4\text{@CeO}_2$ with oxygen vacancies was reduced by H_2 at 500°C for 6 h. The hollow structure can enhance the light efficiency. The heterostructures with oxygen vacancies can result in improved charge separation and interfacial charge transfer efficiency. And thus, a higher degree of utilization is expected to result of enhanced photocatalytic performance for CO_2 under visible light.

2. Experimental section

2.1. Preparation of the $\text{SiO}_2\text{@SiO}_2$

4.35 mL aqueous ammonia (32 wt %) were put into mixed solution of 74 mL ethanol and 10 mL ultrapure water. 5.6 mL TEOS were added to the above mixed solution with magnetic stirring after stirring 30 min at normal atmospheric temperature. Then the mixture were stirred for 1 h to form opal solution. The mixture containing 6.2 mL of TEOS and 3 mL of C_{18}TMOS was added dropwise to the above opal solution with vigorous stirring. After stirring for 3 h, the product was collected, washed, dried at 60°C , and calcined at 550°C for 6 h in air. The prepared $\text{SiO}_2\text{@SiO}_2$ templates include dense nucleus and loose shell, and the thickness of this shell can be adjusted by changing the amounts of TEOS

and C_{18}TMOS . The $\text{SiO}_2\text{@SiO}_2$ template were neutralized with hydrochloric acid.

2.2. Preparation of $\text{SiO}_2\text{@SiO}_2\text{/g-C}_3\text{N}_4$

2 g prepared templates were diffuse into 9 mL cyanamide then stirred for 3 h. Subsequently, the solution was exposed to ultrasound wave about 30 min at 60°C , then heated to 550°C under the flowing N_2 for 4 h with a ramp rate of 5°C min^{-1} . The obtained yellow samples were ground for 10 min, and then $\text{g-C}_3\text{N}_4$ was diffuse into the loose shell.

2.3. Preparation of $\text{g-C}_3\text{N}_4\text{@CeO}_2$ hollow mesospheres

0.4 g of the above prepared sample, 0.15 g L-cysteine and 1 g PVP were diffuse into 80 mL ultrapure water after the application of ultrasound wave for 30 min, and the mixture was treated by oil bath at 95°C . 10 mL 1 mmol $\text{Ce}(\text{NO}_3)_3\text{·}6\text{H}_2\text{O}$ and 10 mL 1 mmol HMTA aqueous solution were added into the above solution under the reflux. After stirring for 2 h, the mixture was cooled down to room temperature, washed several times and dried at 60°C . The products were heated at 550°C for 2 h under the flowing N_2 with a ramp rate of 5°C min^{-1} . The products were dispersed in 30 mL 4 M NH_4HF_2 for 0.5 h to remove the template. The products were centrifuged, washed several time and dried at 60°C . Finally, $\text{g-C}_3\text{N}_4\text{@CeO}_2$ hollow structures were obtained after the samples were heated at 500°C for 6 h under H_2 . The $\text{g-C}_3\text{N}_4$ and hollow CeO_2 with rich oxygen vacancies are fabricated as references with the same methods above.

The characterization and evaluation of photocatalytic properties for CO_2 reduction under visible light are given in the supporting information.

3. Results and discussion

3.1. Structure and morphology of $\text{g-C}_3\text{N}_4\text{@CeO}_2$ hollow photocatalysts

The XRD patterns of the synthesized $\text{g-C}_3\text{N}_4\text{@CeO}_2$ with different CeO_2 contents, pristine $\text{g-C}_3\text{N}_4$ and hollow CeO_2 references are shown

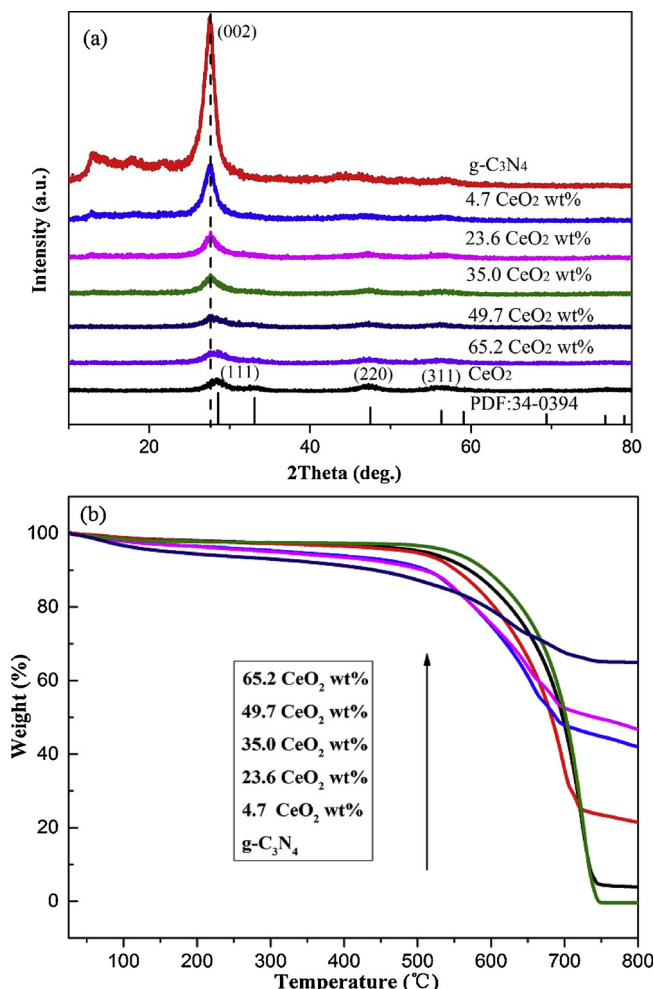


Fig. 2. XRD (a) and TGA (b) pattern of the synthesized hollow g-C₃N₄, hollow CeO₂ references, and g-C₃N₄@CeO₂ samples with different mass ratios.

in Fig. 2a. As it can be seen, all peaks of the aforementioned products are readily indexed in CeO₂ (PDF: 43-0394) and g-C₃N₄, suggesting the successful fabrication of g-C₃N₄@CeO₂ composites and no side-products formed during the synthesis process. The CeO₂ contents in the prepared g-C₃N₄@CeO₂ composites are determined by the thermogravimetric Analysis (TGA), as shown in Fig. 2b, which are 4.7%, 23.6%, 35.0%, 49.7% and 65.2% (wt %), respectively. It is noteworthy that the angle corresponding to (200) crystal face of CeO₂ showed a little shift to those of Ce₂O₃, implying the H₂ reduction led to more oxygen vacancies for the samples. Investigation of broadening corresponding to (111) peak according to Scherrer equation, displayed existing of small particles with the average size ca. 3.5 nm, implying the reduced hollow g-C₃N₄@CeO₂ particles contained nanocrystal subunits. The g-C₃N₄ exhibits two distinct peaks at 27.5° and 13.1°, which are assigned to the (002) and (100) interlayered reference. For the hybrids of g-C₃N₄@CeO₂, the patterns show the combination of two sets of diffraction results containing CeO₂ and g-C₃N₄. With the increase of CeO₂ loading, the intensity of g-C₃N₄ peaks becomes weaken.

SEM images of the dense SiO₂ template and SiO₂@SiO₂ (dense nucleus @ loose shell) are shown as in Fig. 3a and b. The prepared template and SiO₂@SiO₂/g-C₃N₄ are uniformly nanospheres with average sizes of 300 nm and 400 nm. The hybrid SiO₂@SiO₂/g-C₃N₄ shows a rough surface, where the g-C₃N₄ coating layer shows a thickness of around 50 nm, according to the broken particle as inserted in the Fig. 3c. The split in some nanospheres might be caused by rapid mass-transport across the shells. The unique hollow core-shell structure of final product g-C₃N₄@CeO₂ (CeO₂ 49.7 wt %) are also investigated by

SEM and TEM (Fig. 3d–e). The visible hollow interior frame can be observed distinctly and the thickness of the shell can be calculated about 70 nm, which is thicker than that of pristine g-C₃N₄ resulted from the coupled CeO₂ layers. The g-C₃N₄ displays an amorphous nature as expected, which is uniformly attached with CeO₂. HRTEM micrograph (Fig. 3f) of the surface of the sample also shows the lattice spacing of 0.28 nm and 0.31 nm, corresponding to the (200) and (111) plane spacing of CeO₂, which is in agreement with XRD results. The individually synthesized CeO₂ presents a nanoparticle aggregation as shown in Figure S1, which is not as dispersive as the prepared g-C₃N₄@CeO₂ product. The main reason could be attributed to the amino groups of g-C₃N₄ anchored Ce precursors, and meanwhile the existing electrostatic attraction between the negative charge g-C₃N₄ and the Ce cations is also beneficial for stabilizing the Ce source. Therefore, nucleation centers of Ce are dispersive and CeO₂ presents confined growth with g-C₃N₄. The elemental mapping images (Fig. 3g) ascertain the coexistence of Ce, C, N and O in the prepared hollow g-C₃N₄@CeO₂ products. The FTIR spectra of the prepared g-C₃N₄@CeO₂ with different concentrations are shown in Fig. 4. The peaks ranged of 1240–1600 cm⁻¹ can be assigned to the characteristic vibration peaks of C–N heterocyclics in g-C₃N₄. While the peaks under 1000 cm⁻¹ are assigned to metal–oxygen bond [25,26]. These results are in consistent with XRD analysis and previous reports [25–30].

To investigate the surface composition and chemical state of the g-C₃N₄@CeO₂ hollow photocatalysts, XPS analyses of the g-C₃N₄@CeO₂ (CeO₂ 49.7 wt %) are shown in Fig. 5. The survey XPS spectra (Fig. 5a) provide the C 1 s and N 1 s peaks for g-C₃N₄, as well as Ce 3d peak for CeO₂. As shown in Fig. 5b, the C 1 s peak at 284.78 eV, which is assigned to sp² C–C bonds of graphitic carbon [31]. The peaks at 286.24 eV and 288.82 eV are attributed to N–C=N and π-excitation, respectively. These peaks show a slight shift to the higher energy compared with pristine g-C₃N₄, which trend is as the same as other reported results [32,33]. The N 1 s spectra (Fig. 5c) are deconvoluted into two peaks at about 399.16 eV and 401.26 eV, which are corresponding to the SP²-hybridized nitrogen in N–C=N groups and the amino function groups [33]. To confirm the state of Ce, the comparison of the fitted-resolution spectra of hollow g-C₃N₄@CeO₂ before and after H₂ reduction is shown in Fig. 5d. Both samples show various profile natures, which resulted in the deconvolution of peaks into, respectively, five and four doublets of 3d_{5/2} and 3d_{3/2} spin-orbit couples of Ce 3d. The peaks for the g-C₃N₄@CeO₂ before H₂ reduction are fitted at about 880.58 (Ce1), 882.38 (Ce2), 884.18/885.99 (Ce3), 888.96 (Ce4), 898.30 (Ce5), 900.96 (Ce6), 902.86 (Ce7), 907.08 (Ce8), 916.70 (Ce9) eV. The peak of Ce(6) should be assigned to the impurity in CeO₂, which is in agreement with other reports [34,36,37]. The spin orbit doublets for g-C₃N₄@CeO₂ before H₂ reduction show main peaks at binding energies of 898.3 eV (Ce5) and 916.7 eV (Ce9) for Ce⁴⁺ 3d_{5/2} and Ce⁴⁺ 3d_{3/2}, respectively. The peaks located at binding energies of 902.86 eV (Ce7) and 882.38 eV (Ce2) can be attributed to Ce³⁺ 3d_{3/2} and Ce³⁺ 3d_{5/2}, respectively. Two additional peaks at 907.08 eV and 888.96 eV are indicative of orbital “shake-up” of Ce³⁺ 3d_{3/2} and Ce³⁺ 3d_{5/2}, respectively [38–40]. In case of g-C₃N₄@CeO₂ after H₂ reduction, the addition of Ce₂O₃ has brought about slight changes in the binding energy. The characteristic peaks of Ce³⁺ are found at 882.67 eV and 904.28 eV, due to 3d_{5/2} and 3d_{3/2} spin orbit states. While for Ce⁴⁺, the signals are observed at 898.89 eV (3d_{5/2}), 917.16 eV (3d_{3/2}) [40–42]. The weak peaks of Ce (3) 884.18 and 885.99 eV should be assigned to the Ce³⁺, merged together a strong peak after H₂ reduction. The peak areas of Ce (3) distinctly enhance and the peak stations shift to a higher value after H₂ reduction because the partial Ce⁴⁺ is reduced to Ce³⁺. Therefore, the concentration of Ce³⁺ improves and the decreased charges in valence band enhance the binding energy [34,35,43]. The N₂ adsorption/desorption isotherms and the pore size distribution of the obtained g-C₃N₄@CeO₂ (CeO₂ 49.7 wt %) product is shown in Fig. 6. The N₂ adsorption/desorption isotherms of pristine hollow g-C₃N₄ and CeO₂ are shown in Figure S2 and S3 in Supporting Information. The

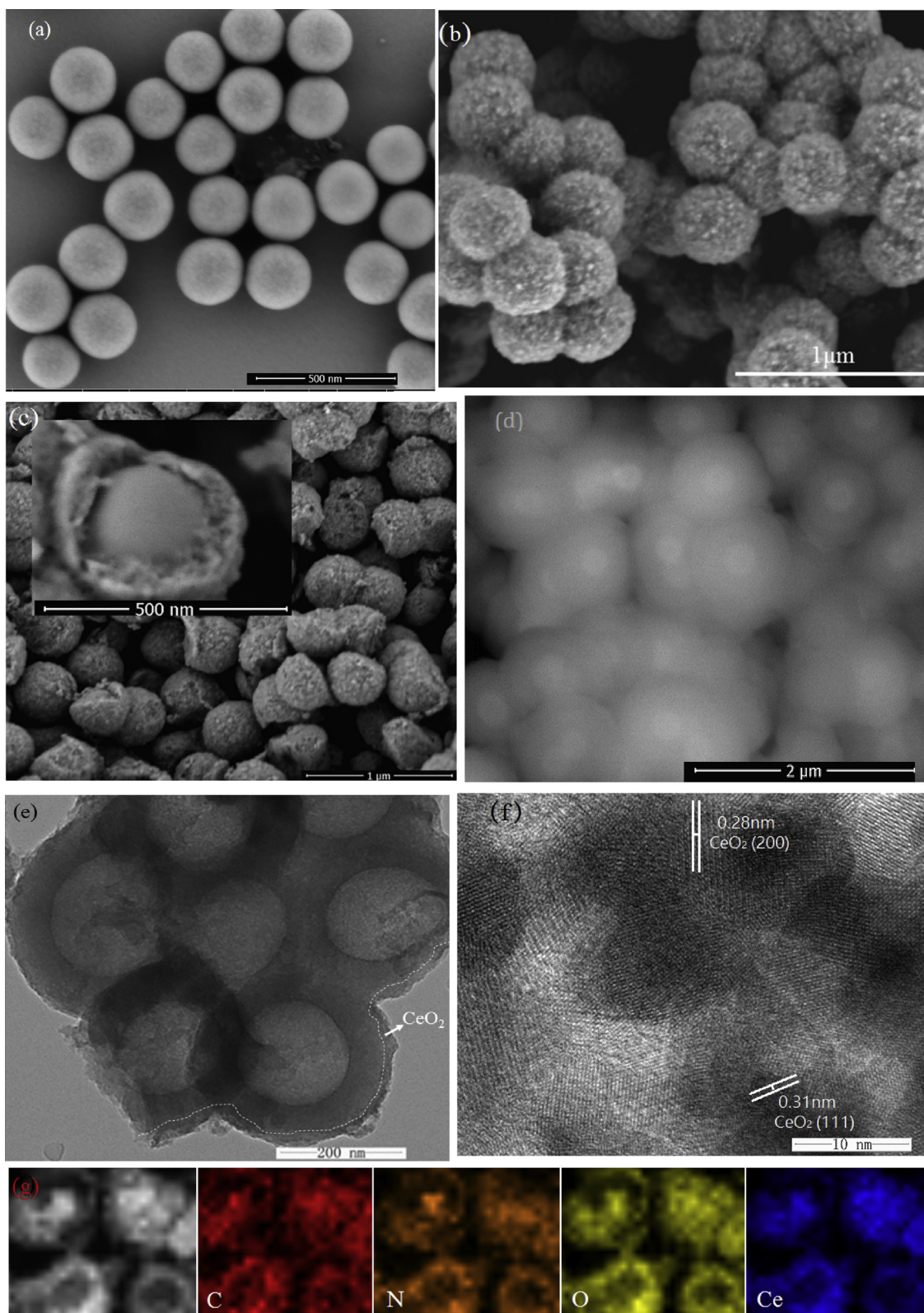


Fig. 3. (a) SEM images of the dense SiO₂, (b) SiO₂@SiO₂ with dense nucleus and loose shell, and (c) SiO₂@SiO₂/g-C₃N₄. (d) SEM, (e) TEM morphology, (f) HRTEM micrograph, and (g) EDX mapping images (the element of C, N, O, Ce) of the fabricated of g-C₃N₄@CeO₂ (CeO₂ 49.7 wt %).

isotherm is identified as type IV, which is the characteristic isotherm of mesoporous materials. The BET surface area of g-C₃N₄@CeO₂ (CeO₂ 49.7 wt %) product is 125.1 m² g⁻¹, which is larger than most of currently reported g-C₃N₄ and CeO₂ based photocatalysts and is beneficial for CO₂ adsorption. Therefore, this unique hollow structured

heterojunction is expected to be favorable for enhanced reduction of CO₂ in the process of photocatalytic reaction.

Electron paramagnetic resonance (EPR) spectroscopy is well suited to examine the nature of the oxidation state (Ce⁴⁺/Ce³⁺) of CeO₂ nanostructures, which exhibits weak room temperature ferromagnetism.

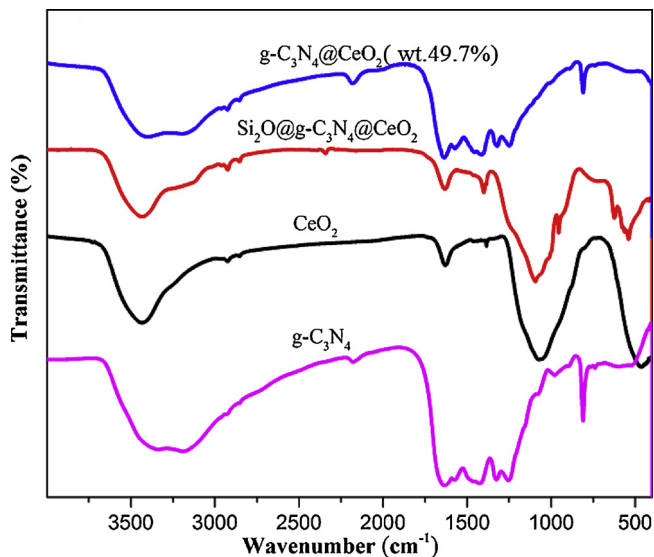


Fig. 4. FTIR spectra of the synthesized hollow g-C₃N₄, hollow CeO₂ references, and g-C₃N₄@CeO₂ samples.

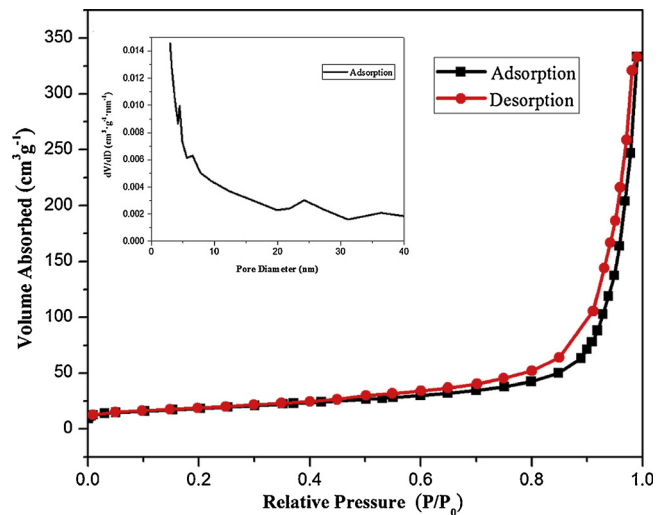


Fig. 6. Nitrogen adsorption/desorption isotherms of as-prepared g-C₃N₄@CeO₂.

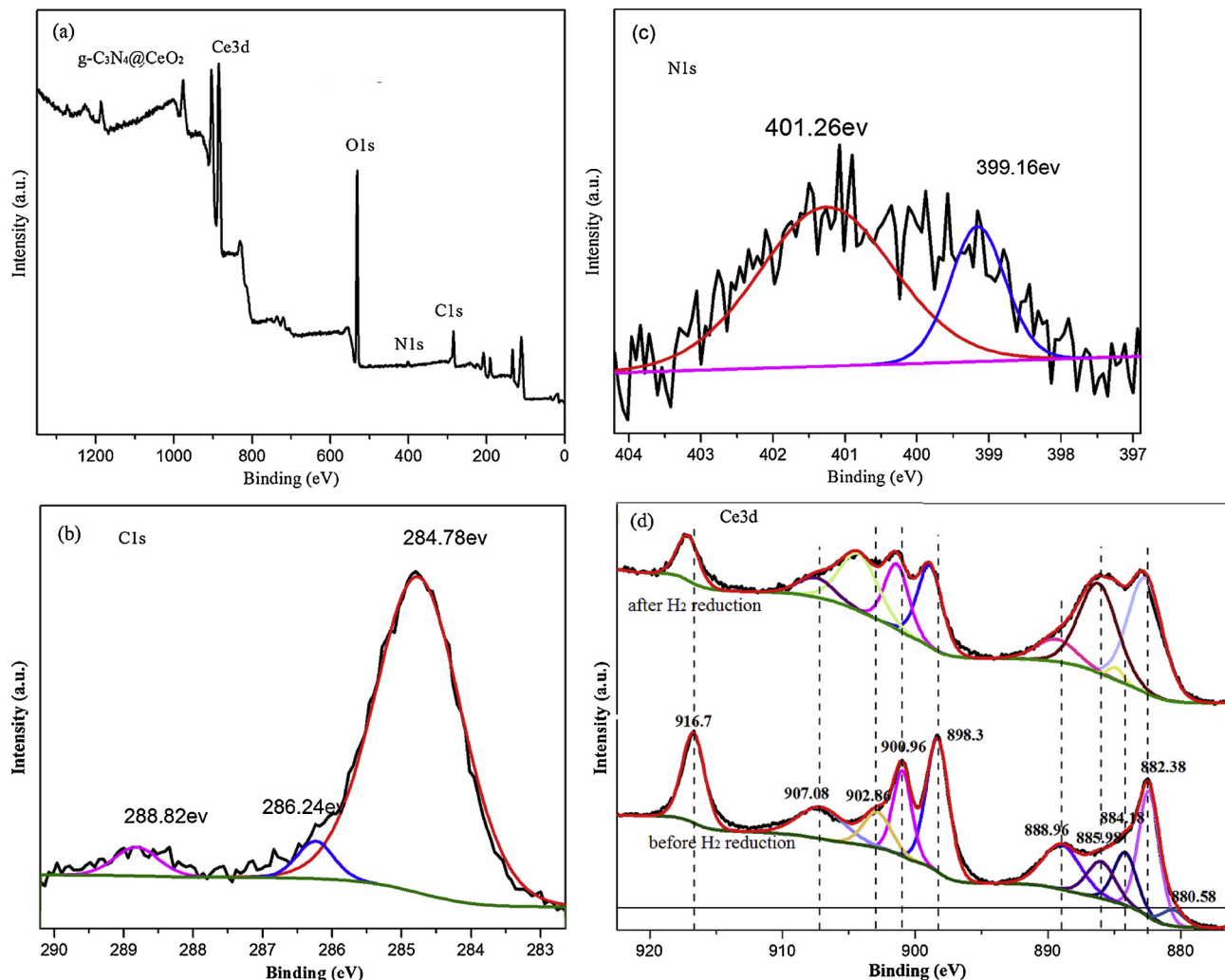


Fig. 5. XPS spectra of the as-prepared g-C₃N₄@CeO₂ sample: (a) survey spectrum, (b) C 1s spectrum, (c) N 1s spectrum, (D) The Ce 3d spectrum of g-C₃N₄@CeO₂ before and after H₂ reduction.

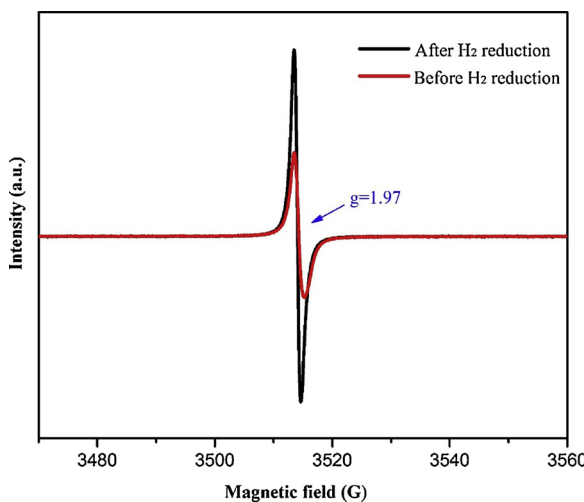


Fig. 7. EPR spectra of hollow $\text{g-C}_3\text{N}_4@\text{CeO}_2$ hybrid structures before and after H_2 reduction at room temperature with a 100 kHz modulation frequency.

Therefore, we analyzed the EPR spectrum at room temperature with a 100 kHz modulation frequency as shown in Fig. 7. EPR spectrum detected obvious signals for the oxygen vacancy of CeO_2 after H_2 reduction, whereas the CeO_2 before H_2 reduction exhibited the weak EPR signals. The previous reports prove that the EPR detection of Ce^{3+} ions in CeO_2 relates mainly to the line with $g = \sim 1.97$ at room and up to very high temperatures [36], which is not typical for rare-earth ions and rather close to the g value of cubic site position of Ce^{3+} in CeO_2 particles. The trigonal site of the Ce^{3+} ion can be easily realized near an oxygen vacancy [34–37,43]. The prepared hollow $\text{g-C}_3\text{N}_4@\text{CeO}_2$ hybrid structures showed the obvious single EPR signal, belonging to oxygen vacancies, while weak EPR signal appears in the case of CeO_2 samples before H_2 reduction. Therefore, EPR showed that the hollow $\text{g-C}_3\text{N}_4@\text{CeO}_2$ hybrid structures have characteristic oxygen vacancies, which could impart visible light-induced photocatalytic activity [34–37,38].

3.2. Formation of $\text{g-C}_3\text{N}_4@\text{CeO}_2$ hollow photocatalysts with controlled morphologies

We analyze the formation of $\text{g-C}_3\text{N}_4@\text{CeO}_2$ hollow structures, illustrated in Fig. 1. Briefly, SiO_2 (compact)@ SiO_2 (loose) acted as template as shown Fig. 2b. The silica is etched by NH_4HF_2 after the formation of $\text{SiO}_2@\text{g-C}_3\text{N}_4@\text{CeO}_2$. Subsequently, a high-temperature H_2 reducing process was applied for fabricating the hollow $\text{g-C}_3\text{N}_4@\text{CeO}_2$ photocatalysts with rich oxygen vacancies. Our strategy provides a general designed route to fabricate hollow structured $\text{g-C}_3\text{N}_4$ based photocatalysts and this designed strategy can also be used to prepare other advanced yolk-shell materials, such as $\text{g-C}_3\text{N}_4@\text{SnS}$ (Figure S4) and $\text{g-C}_3\text{N}_4@\text{TiO}_2$ (Figure S5). All of them show excellent performance in the field of environmental catalysis and energy storage.

3.3. Optical properties

UV-vis absorption band edges of products of pristine $\text{g-C}_3\text{N}_4$, CeO_2 and $\text{g-C}_3\text{N}_4@\text{CeO}_2$ coupled photocatalysts contained CeO_2 concentration of 4.7%, 23.6%, 35.0%, 49.7% and 65.2% (wt %) samples are shown in Fig. 8. UV-vis absorption band edges of the samples with CeO_2 concentration of 41.2%, 45.6% and 55.2% are listed in Figure S6 (Supporting Information). The visible photoabsorption intensity enhanced prominently with the increase of the content of CeO_2 . Particularly, the $\text{g-C}_3\text{N}_4@\text{CeO}_2$ (CeO_2 49.7 wt %) presents the significant red shift. The band energy (E_g value) of hollow $\text{g-C}_3\text{N}_4$, and hollow CeO_2 are 2.70 and 2.93 by Tauc relation, respectively. So, they can be

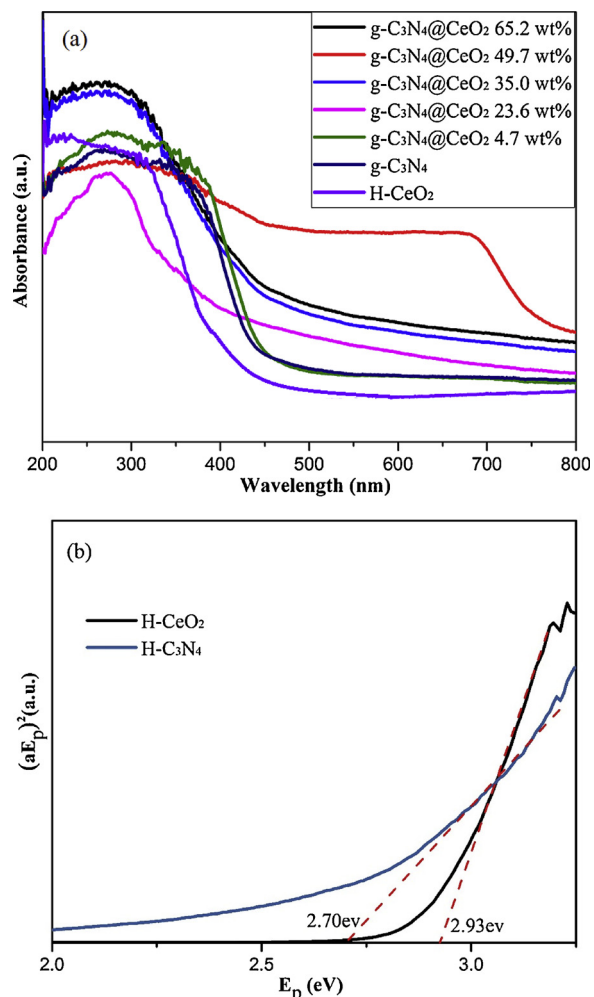


Fig. 8. UV-vis diffuse reflectance spectrum (a) of pristine hollow $\text{g-C}_3\text{N}_4$, hollow CeO_2 references, and $\text{g-C}_3\text{N}_4@\text{CeO}_2$ samples with different ratios and the plots of $(aE_p)^2$ versus energy ($h\nu$) for the band gap energies of the samples (b).

promisingly acted as visible light photocatalysts. Narrowing in the band gap of the prepared CeO_2 and $\text{g-C}_3\text{N}_4$ occurs because of the formation of hollow structure, which is supported by XPS studies and also in good conformity with other researches [24–30]. The band gap narrowing displays more efficient utilization of solar spectrum and consequently more photoinduced charge generation to exert superior photocatalytic performance.

3.4. Photocatalytic activity and mechanism for CO_2 reduction

The maximum CO_2 adsorption capabilities of the CeO_2 , $\text{g-C}_3\text{N}_4$ and $\text{g-C}_3\text{N}_4@\text{CeO}_2$ (CeO_2 49.7 wt %) are 0.25, 0.16, and $0.31 \mu\text{mol g}^{-1}$ as illustrated Table 1, revealing the $\text{g-C}_3\text{N}_4@\text{CeO}_2$ (Ce 49.7 wt %) exhibits the highest value in the three samples. The enhanced CO_2 adsorption capacity plays an important role in the conversion of CO_2 to

Table 1

The maximum CO_2 adsorption capabilities and specific surface areas for the hollow CeO_2 , $\text{g-C}_3\text{N}_4$ references and $\text{g-C}_3\text{N}_4@\text{CeO}_2$ (CeO_2 49.7 wt %).

Sample	S_{BET} ($\text{m}^2 \text{g}^{-1}$)	CO_2 adsorption (mmol g^{-1})
CeO_2	146.8	0.25
$\text{g-C}_3\text{N}_4$	63.9	0.16
oxygen vacant $\text{g-C}_3\text{N}_4@\text{CeO}_2$	125.1	0.31

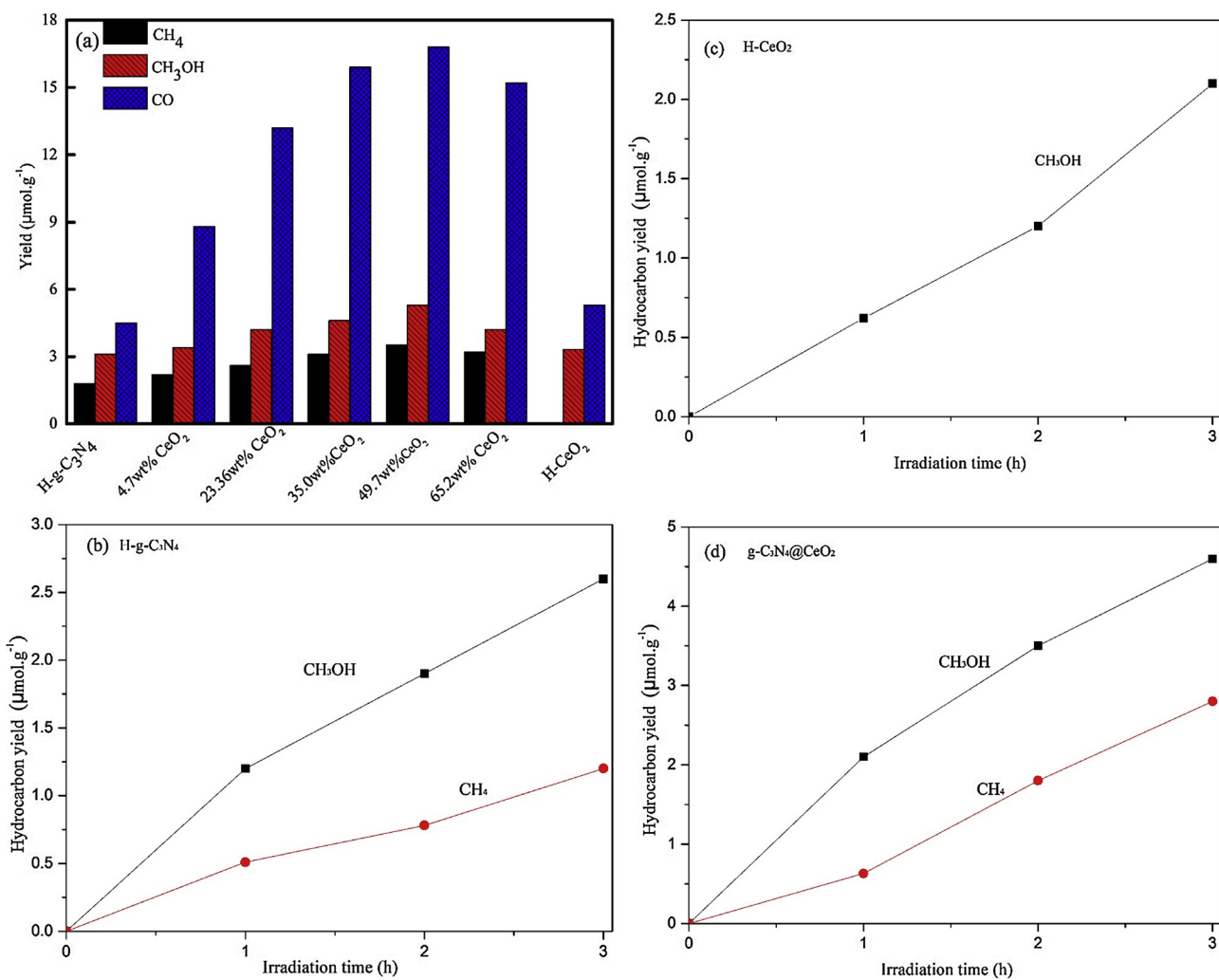


Fig. 9. (a) Hydrocarbon generation rate in comparison with samples of hollow $\text{g-C}_3\text{N}_4$, hollow CeO_2 , and $\text{g-C}_3\text{N}_4@\text{CeO}_2$ for 4 h illumination. (b-d) Time courses of photocatalytic CH_4 and CH_3OH production over the prepared different samples under visible light irradiation for 3 h.

hydrocarbons [6,44]. The L-cysteine offered the amine groups and meanwhile anchored on the surface of $\text{g-C}_3\text{N}_4$ during the synthesis process, and thus contributes greatly to the enhanced CO_2 adsorption performance. In fact, this pathway has been widely adopted to improve the CO_2 adsorption capacity of materials because of their large content of alkalinity [45]. The photocatalytic CO_2 reduction is conducted with a 420 nm cutoff filter as the visible light source. The results show that no hydrocarbons can be detected in the absence of photocatalysts or irradiation, indicating that effective photocatalysts and illumination are two essential factors for photocatalytic CO_2 reduction. The photocatalytic activities of $\text{g-C}_3\text{N}_4$, CeO_2 , $\text{g-C}_3\text{N}_4@\text{CeO}_2$ for CO_2 reduction under visible-light irradiation are shown in Fig. 9a. The main photocatalytic products are important storable fuels of CO , CH_3OH and CH_4 . The reduction products of CH_3OH and CH_4 involved more electrons transfer and relative energies according to Table S1. The evolution rate of the CO is significantly faster than that of other products, which is ascribed to a faster kinetics of their reduction reactions. Therefore, the relative reaction is more difficult to be occurred compared with CO . (see Supporting Information) The analysis of apparent quantum efficiency (AQE) is shown in Supporting Information. The change of CH_4 of 4 h photoreaction under different monochromatic light wavelengths at 525 nm were measured as reference, because the CH_4 production is most difficult and its efficiency is the lowest in the reduction products. The energy flux (mW cm^{-2}) of the Xe lamp was measured with a calibrated Si photodiode, and the photon flux absorbed by photocatalyst

was obtained by dividing the energy flux by the energy of a photon with a wavelength of 525 nm. The apparent quantum efficiencies (AQE) was measured to be around 17.1%

It is noticed that the CH_4 is not detected in the photocatalytic reduction products for individual hollow CeO_2 with oxygen vacancies, and the yields of CO and CH_3OH are 5.3 and $3.3 \mu\text{mol g}^{-1}$, respectively. Though the pristine hollow $\text{g-C}_3\text{N}_4$ exhibits lower BET surface areas, weaker CO_2 adsorption capacity compared with CeO_2 , it shows better CO_2 reduction effect with the yields of CH_4 and CH_3OH are 1.8 and $3.1 \mu\text{mol g}^{-1}$, implying the hollow $\text{g-C}_3\text{N}_4$ possesses intrinsic pre-eminent charge separation and transfer effect for the photoexcitation during the CO_2 photocatalytic reduction. However, the relative high CB position and rapid electron-hole recombination of CeO_2 alone should be responsible for its inferior reduction ability of CO_2 . Particularly, the hollow $\text{g-C}_3\text{N}_4@\text{CeO}_2$ hybrids exhibit obviously enhanced photocatalytic CO_2 reduction. With the increase of CeO_2 content, the reduction performance of CO_2 remarkably increases and subsequently decreases. The $\text{g-C}_3\text{N}_4@\text{CeO}_2$ (Ce 49.7 wt %) delivered the highest yields of CH_4 ($3.5 \mu\text{mol g}^{-1}$), CH_3OH ($5.2 \mu\text{mol g}^{-1}$) and CO ($16.8 \mu\text{mol g}^{-1}$), which are higher than most of other latest reported $\text{g-C}_3\text{N}_4$ based photocatalysts for CO_2 photoreduction including coupled with semiconductors and noble metal cocatalysts [24–30].

To demonstrate the CH_4 and CO are derived from CO_2 , three control experiments and an isotopic experiment with $^{13}\text{CO}_2$ were conducted: (1) experiment with $\text{g-C}_3\text{N}_4@\text{CeO}_2$, CO_2 and water, but without light

irradiation; (2) experiment with CO_2 , water and light irradiation, but without $\text{g-C}_3\text{N}_4@\text{CeO}_2$; and (3) experiment with $\text{g-C}_3\text{N}_4@\text{CeO}_2$, water, and light irradiation, but without CO_2 . No appreciable amounts of CO and CH_4 are detected in all of the three control experiments, implying that CO and CH_4 are generated by the photocatalytic reduction of CO_2 on the $\text{g-C}_3\text{N}_4@\text{CeO}_2$. In the isotopic experiment using $^{13}\text{CO}_2$, the generated products are analysed as ^{13}CO and $^{13}\text{CH}_4$ by gas chromatography-mass spectrometry (GC-MS). Additionally, the Ar is employed to replace CO_2 while keeping the other experimental conditions are the same as those for CO_2 reduction, and no CO and CH_4 are detected, which further demonstrates that CO and CH_4 are derived from the photocatalytic CO_2 reduction on $\text{g-C}_3\text{N}_4@\text{CeO}_2$.

Because the photocatalytic reductions to generate CH_4 and CH_3OH are more difficult to be occurred compared with CO , we analysis the course of products of CH_4 and CH_3OH with different reaction time to investigate the photocatalytic mechanism under visible light as shown Fig. 9b-d. For hollow $\text{g-C}_3\text{N}_4$, both CH_3OH and CH_4 generate initially under visible light irradiation. While for hollow CeO_2 , only CH_3OH is detected from the initial time, however, the CH_4 is not detected during the whole testing period. As for $\text{g-C}_3\text{N}_4@\text{CeO}_2$ (CeO_2 49.7 wt %), both CH_3OH and CH_4 generate in the beginning. Particularly, the content of CH_4 and CH_3OH continuously increases obviously with the time prolongation and the yield even arrives at as high as 2.8 and $4.6 \mu\text{mol g}^{-1}$, respectively. These values are much higher than that of pristine hollow $\text{g-C}_3\text{N}_4$ and CeO_2 . With regard to the different results of the samples corresponding to different ratios for CO_2 reduction, many factors should be responsible for the photocatalytic activity. According to the analysis above, among these influencing factors, the size, morphology and specific surface area are almost the same. Additionally, the maximum CO_2 adsorption capabilities of $\text{g-C}_3\text{N}_4@\text{CeO}_2$ is no higher than that of CeO_2 significantly. Therefore, it can be assumed that the $\text{g-C}_3\text{N}_4@\text{CeO}_2$ heterojunctions and oxygen vacancies play the major roles in the photocatalytic reduce reaction. In fact, $\text{g-C}_3\text{N}_4$ exists the visible light response range and has higher photocatalytic activity compared with CeO_2 . However, the separation efficiency of photoinduced electron-hole pairs of $\text{g-C}_3\text{N}_4$ is poor. CeO_2 can more effectively inhibit the recombination of photoinduced charge carrier pairs compared with $\text{g-C}_3\text{N}_4$. The two semiconductors have suitable band potential and can form the hetero-junction structure to suppress the recombination of electron-hole pairs. More content of CeO_2 implies more amounts of CeO_2 existing $\text{g-C}_3\text{N}_4@\text{CeO}_2$ heterojunctions, which can well explain why the photocatalytic efficiency improved with increasing of CeO_2 content. However, it doesn't mean that the higher CeO_2 content loads, the better photocatalytic performance can be obtained. The high contents of CeO_2 on the surface of $\text{g-C}_3\text{N}_4@\text{CeO}_2$ heterojunctions may hinder light irradiation on $\text{g-C}_3\text{N}_4$ and limit the mutual contact between CO_2 and $\text{g-C}_3\text{N}_4$. So further increasing the content of CeO_2 leads to decreased photocatalytic efficiency. Meanwhile, more $\text{g-C}_3\text{N}_4$ in the $\text{g-C}_3\text{N}_4@\text{CeO}_2$ is also not beneficial for the photocatalytic performance. The main reason is that too low CeO_2 in the heterojunctions may confine interfacial electron transfer from $\text{g-C}_3\text{N}_4$ to CeO_2 . So the reduction efficiency of CO_2 decreases if the content of $\text{g-C}_3\text{N}_4$ is excessive loading according to Fig. 9a. Therefore, an appropriate composition of $\text{g-C}_3\text{N}_4@\text{CeO}_2$ heterojunctions accomplishes the satisfied photocatalytic performance, and the $\text{g-C}_3\text{N}_4@\text{CeO}_2$ (CeO_2 49.7 wt %) presents the best photocatalytic activity. Based on the results above, it is reasonable that the photoinduced electrons transfer to and accumulate on the CeO_2 surface, resulting in the generation of CH_4 . The generation of CH_4 needs much more electrons compared with the formation of CH_3OH . As for $\text{g-C}_3\text{N}_4@\text{CeO}_2$ photocatalyst, the synergistic effect of mutual activations should be responsible for the effectively gathering of the photoinduced electrons, leading to generate CH_4 much earlier and higher concentration than that of the pristine $\text{g-C}_3\text{N}_4$. Meanwhile, the rate of CH_4 formation becomes fast with illumination time prolongation.

The interactions between the $\text{g-C}_3\text{N}_4$ and CeO_2 contribute greatly to the separation electron-hole pairs and thus has significant effect on its

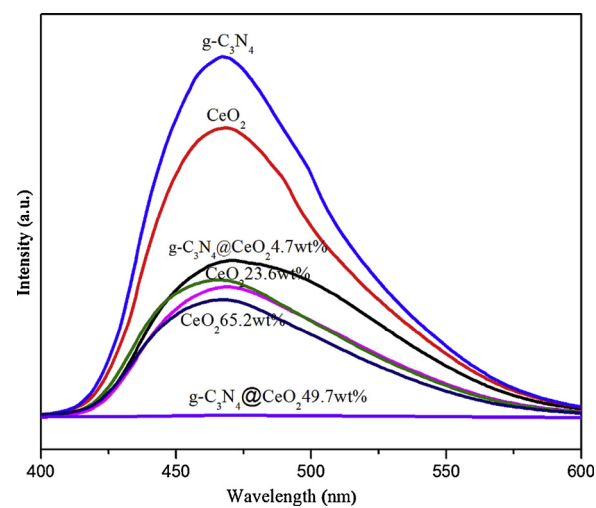


Fig. 10. Photoluminescence spectra of hollow $\text{g-C}_3\text{N}_4$, hollow CeO_2 references, and $\text{g-C}_3\text{N}_4@\text{CeO}_2$ samples with different ratios.

photocatalytic activity. Therefore, Photoluminescence (PL) spectra is applied to prove the enhanced separation efficiency of electron-hole pairs as shown in Fig. 10. The pristine hollow $\text{g-C}_3\text{N}_4$ shows a strong emission peak centered at about 460 nm, which is ascribed to the recombination of self-trapped excitons. The emission band becomes lower with the increasing content of CeO_2 . The enhanced separation efficiency of electron-hole pairs leads to the decrease of peak intensity. The $\text{g-C}_3\text{N}_4@\text{CeO}_2$ (CeO_2 49.7 wt %) presents the best separation efficiency, which is coincided well with the photocatalytic performance. Surface photovoltage spectroscopy (SPS, Fig. 11) is performed to further investigate the enhanced separation efficiency of the photoinduced electron-hole pairs. In principle, the strong SPS response is in line with the high separation efficiency of the photo-induced carriers on the basis of the SPS technology [46]. From Fig. 11, all the samples exhibit relative obvious SPS signal in visible light region, and the $\text{g-C}_3\text{N}_4@\text{CeO}_2$ (CeO_2 49.7 wt %) displays the most intensive SPS responses. These results imply that the heterostructure of $\text{g-C}_3\text{N}_4@\text{CeO}_2$ is beneficial to improve the separation efficiency of photoinduced charge carriers.

Based on the above analysis and combined with the former calculated band energy (E_g value) of samples, the transfer pathway of photoinduced carriers is presented in Fig. 12, which shows the schematic illustration of band structure diagram of $\text{g-C}_3\text{N}_4@\text{CeO}_2$. The E_g of $\text{g-C}_3\text{N}_4$ and CeO_2 is 2.7 and 2.93 eV. The VB edges of CeO_2 and $\text{g-C}_3\text{N}_4$ are calculated as 2.47 and 1.45 eV [29]. The valence band X-ray photoelectron spectroscopy were measured using PHI5000 Veras Probe

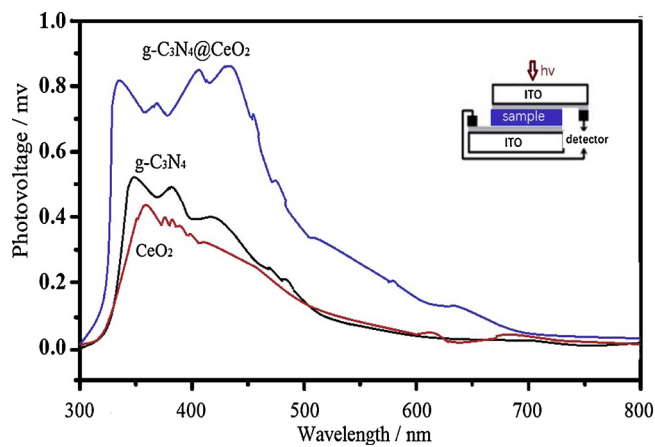


Fig. 11. Surface photovoltage spectroscopy of hollow CeO_2 , $\text{g-C}_3\text{N}_4$ references and $\text{g-C}_3\text{N}_4@\text{CeO}_2$ (CeO_2 49.7 wt %).

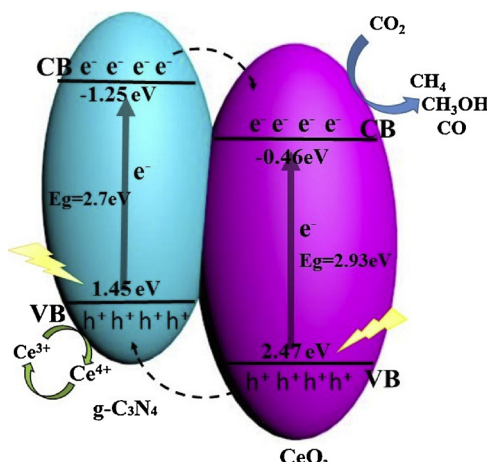


Fig. 12. Schematic illustration of band structure diagram and photoinduced carriers transfer of $\text{g-C}_3\text{N}_4@\text{CeO}_2$ under visible light irradiation.

instrument. The 2.40 eV and 1.52 eV are corresponding to the VB position of CeO_2 and $\text{g-C}_3\text{N}_4$ as shown in Figure S7 in the Supporting Information, respectively, which is near the analysis above. So that, the CB potentials of CeO_2 and $\text{g-C}_3\text{N}_4$ are calculated as -0.46 and -1.25 eV according to $E_{\text{CB}} = E_{\text{VB}} - E_g$, which values are more negative than the reduction potentials of the formation of CH_4 , CH_3OH and CO . However, the CH_4 has not been detected in the products for the CeO_2 alone even after 3 h, implying the accumulation and extraction of photoinduced electrons are not offered because of fast charge recombination. For the $\text{g-C}_3\text{N}_4@\text{CeO}_2$ composites, the photogenerated electrons in the CB of $\text{g-C}_3\text{N}_4$ will migrate to that of the CeO_2 while the holes generated in the CeO_2 transfer to the VB of the $\text{g-C}_3\text{N}_4$. Such interfacial electron transfer consequently promotes the separation of electron-hole pairs leading to accumulation of electron-hole pairs with longer life-times over the $\text{g-C}_3\text{N}_4@\text{CeO}_2$. At the CB of CeO_2 , CO_2 are reduced to CO , CH_3OH and CH_4 by accumulated photoinduced electrons (e^-). Meanwhile, the accumulated holes (h^+) on the $\text{g-C}_3\text{N}_4$ will lead to partial oxidation of Ce^{3+} to Ce^{4+} (1.44 vs. NHE, at pH = 7), and the photogenerated h^+ has an important role in prolonging the lifetime of the photogenerated charge carriers in $\text{g-C}_3\text{N}_4@\text{CeO}_2$ system via converting Ce^{3+} to Ce^{4+} [26]. It can be noticed Ce^{4+} can trap photo-excited electrons on the interface, and Ce^{3+} can react with gas-phase CO_2 to generate CO_2^- , which can be further reduced to CO and CH_4 [47–49]. Therefore, $\text{g-C}_3\text{N}_4$ coupled with CeO_2 with rich oxygen vacancies photocatalysts can preserve their strong reducibility and promote the photocatalytic CO_2 reduction under visible light irradiation. In addition, the synthesized pristine $\text{g-C}_3\text{N}_4$ and CeO_2 might also facilitate the photo electron-hole recombination due to the narrow energy band gap, leading to the decreased quantum efficiency, and thus exhibits lower photocatalytic activity compared with $\text{g-C}_3\text{N}_4@\text{CeO}_2$. Moreover, the unique hollow structure can make multiple reflections of light in the cavity, and which enhanced the light utilization. The large BET surface areas are also beneficial for the enhanced photocatalytic CO_2 reduction performance. These results indicate that the present hollow $\text{g-C}_3\text{N}_4@\text{CeO}_2$ structures are promising as a broad visible light-harvesting photocatalyst.

4. Conclusions

Hollow heterostructured $\text{g-C}_3\text{N}_4@\text{CeO}_2$ with rich oxygen vacancies has been successfully synthesized by a new general approach. These heterostructures with rich oxygen vacancies can enhance the efficiency of charge separation and transfer. The hollow frame of the photocatalyst improve the light efficiency significantly due to the effective multiple reflections in the chamber. Therefore, a high reduction performance for CO_2 was observed. This work might provide a novel

approach to address the formation and charge transfer mechanism of $\text{g-C}_3\text{N}_4$ based photocatalysts without addition of noble metal for CO_2 photocatalytic reduction.

Acknowledgements

National Natural Science Foundation of China (no.21467030), Key Natural Science Foundation of Yunnan Province China (no.2018FA028), and the Program for Outstanding Young Talents of Yunnan University (no.2018YDJQ003).

Appendix A. Supplementary data

Supplementary material related to this article can be found, in the online version, at doi:<https://doi.org/10.1016/j.apcatb.2018.11.010>.

References

- [1] X. Chang, T. Wang, J. Gong, CO_2 photo-reduction: insights into CO_2 activation and reaction on surfaces of photocatalysts, *Energy Environ. Sci.* 9 (2016) 2177–2196.
- [2] O. Ola, M.M. Maroto-Valer, Review of material design and reactor engineering on TiO_2 photocatalysis for CO_2 reduction, *J. Photochem. Photobiol. C* 24 (2015) 16–42.
- [3] W. Tu, Y. Zhou, Z. Zou, Photocatalytic conversion of $\text{CO}(2)$ into renewable hydrocarbon fuels: state-of-the-art accomplishment, challenges, and prospects, *Adv. Mater.* 26 (2014) 4607–4626.
- [4] K. Li, B. Peng, T. Peng, Recent advances in heterogeneous photocatalytic CO_2 conversion to solar fuels, *ACS Catal.* 6 (2016) 7485–7527.
- [5] H. Bian, Y. Ji, J. Yan, P. Li, L. Li, Y. Li, S. Liu, In situ synthesis of few-layered $\text{g-C}_3\text{N}_4$ with vertically aligned MoS_2 loading for boosting solar-to-hydrogen generation, *Small* 14 (2018) 1703003–1703011.
- [6] T. Di, B. Zhu, B. Cheng, J. Yu, J. Xu, A direct Z-scheme $\text{g-C}_3\text{N}_4/\text{SnS}_2$ photocatalyst with superior visible-light CO_2 reduction performance, *J. Catal.* 352 (2017) 532–541.
- [7] M. Liang, T. Borjigin, Y. Zhang, H. Liu, B. Liu, H. Guo, Z-scheme $\text{Au}/\text{Void}/\text{g-C}_3\text{N}_4/\text{SnS}$ yolk-shell heterostructures for superior photocatalytic CO_2 reduction under visible light, *ACS Appl. Mater. Interfaces* 10 (2018) 34123–34131.
- [8] W.-J. Ong, L.-L. Tan, Y.H. Ng, S.-T. Yong, S.-P. Chai, Graphitic carbon nitride ($\text{g-C}_3\text{N}_4$)-based photocatalysts for artificial photosynthesis and environmental remediation: are we a step closer to achieving sustainability, *Chem. Rev.* 116 (2016) 7159–7329.
- [9] S. Cao, J. Low, J. Yu, M. Jaroniec, Polymeric photocatalysts based on graphitic carbon nitride, *Adv. Mater.* 27 (2015) 2150–2176.
- [10] J. Wen, J. Xie, X. Chen, X. Li, A review on $\text{g-C}_3\text{N}_4$ -based photocatalysts, *Appl. Surf. Sci.* 391 (2016) 72–123.
- [11] N. Tian, H. Huang, Y. He, Y. Guo, T. Zhang, Y. Zhang, Mediator-free direct Z-scheme photocatalytic system: $\text{BiVO}_4/\text{g-C}_3\text{N}_4$ organic-inorganic hybrid photocatalyst with highly efficient visible-light-induced photocatalytic activity, *Dalton Trans.* 44 (2015) 4297–4307.
- [12] W. Yu, D. Xu, T. Peng, Enhanced photocatalytic activity of $\text{g-C}_3\text{N}_4$ for selective CO_2 reduction to CH_3OH via facile coupling of ZnO : a direct Z-scheme mechanism, *J. Mater. Chem. A* 3 (2015) 19936–19947.
- [13] P. Li, Y. Zhou, H. Li, Q. Xu, X. Meng, X. Wang, M. Xiao, Z. Zou, All-solid-state Z-scheme system arrays of $\text{FeVO}/\text{RGO}/\text{CdS}$ for visible light-driving photocatalytic CO reduction into renewable hydrocarbon fuel, *Chem. Commun.* 51 (2014) 800–803.
- [14] N. Nishiyama, K. Kozasa, S. Yamazaki, Photocatalytic degradation of 4-chlorophenol on titanium dioxide modified with Cu(II) or Cr(III) ion under visible light irradiation, *Appl. Catal. A* 527 (2016) 109–115.
- [15] A. Idris, N. Hassan, R. Rashid, A. Ngomsik, Kinetic and regeneration studies of photocatalytic magnetic separable beads for chromium (VI) reduction under sunlight, *J. Hazard. Mater.* 186 (2011) 629–635.
- [16] H. Guo, Y.Y. Guo, L.X. Liu, T.T. Li, W. Wang, W.W. Chen, Designed hierarchical synthesis of ring-shaped $\text{Bi}_2\text{WO}_6@\text{CeO}_2$ hybrid nanoparticle aggregates for photocatalytic detoxification of cyanide, *J. Chen, Green Chem.* 16 (2014) 2539–2545.
- [17] H. Guo, W. Wang, L.X. Liu, Y.B. He, C.P. Li, Y.P. Wang, Shape-controlled synthesis of $\text{Ag}@\text{TiO}_2$ cage-bell hybrid structure with enhanced photocatalytic activity and superior lithium storage, *Green Chem.* 15 (2013) 2810–2816.
- [18] Z. Lv, H. Zhou, H. Liu, B. Liu, M. Liang, Hong Guo, Controlled assemble of oxygen vacant $\text{CeO}_2@\text{Bi}_2\text{WO}_6$ hollow magnetic microcapsule heterostructures for visible-light photocatalytic activity, *Chem. Eng. J.* 330 (2017) 1297–1305.
- [19] C. Karunakaran, P. Gomathisankar, G. Manikandan, Preparation and characterization of antimicrobial Ce-doped ZnO nanoparticles for photocatalytic detoxification of cyanide, *Mater. Chem. Phys.* 123 (2010) 585–594.
- [20] A.D. Liyanage, S.D. Perera, K. Tan, Y. Chabal, K.J.B. Jr, synthesis, characterization, and photocatalytic activity of Y-doped CeO_2 nanorods, *ACS Catal.* 4 (2014) 577–584.
- [21] M. Kurian, C. Kunjachan, $\text{Ce}_x\text{V}_{1-x}\text{O}_2$, ($x:0.0,25–1$) nanocomposites as efficient catalysts for degradation of 2,4 dichlorophenol, *J. Environ. Chem. Eng.* 4 (2016) 1359–1366.
- [22] B. Choudhury, P. Chetri, A. Choudhury, Oxygen defects and formation of Ce^{3+}

affecting the photocatalytic performance of CeO_2 nanoparticles, *RSC Adv.* 4 (2014) 4663–4671.

[23] F.J. López-Tenllado, S. Murcia-López, D.M. Gómez, A. Marinas, J.M. Marinas, F.J. Urbano, J.A. Navío, M.C. Hidalgo, J.M. Gatic, A comparative study of Bi_2WO_6 , CeO_2 , and TiO_2 as catalysts for selective photo-oxidation of alcohols to carbonyl compounds, *Appl. Catal. A* 5 (2015) 375–381.

[24] S. Issarapanacheewin, K. Wetchakun, S. Phanichphant, W. Kangwansupamonkon, N. Wetchakun, Efficient photocatalytic degradation of Rhodamine B by a novel $\text{CeO}_2/\text{Bi}_2\text{WO}_6$ composite film, *Catal. Today* 278 (2016) 280–290.

[25] X. She, H. Xu, H. Wang, J. Xia, Y. Song, J. Yan, Y. Xu, Q. Zhang, D. Du, H. Li, Controllable synthesis of $\text{CeO}_2/\text{g-C}_3\text{N}_4$ composites and their applications in the environment, *Dalton Trans.* 44 (2015) 7021–7031.

[26] M. Li, L. Zhang, M. Wu, Y. Du, X. Fan, M. Wang, L. Zhang, Q. Kong, J. Shi, Mesostructured $\text{CeO}_2/\text{g-C}_3\text{N}_4$ nanocomposites: remarkably enhanced photocatalytic activity for CO_2 reduction by mutual component activations, *Nano Energy* 19 (2016) 145–155.

[27] N. Tian, H. Huang, C. Liu, F. Dong, T. Zhang, X. Du, S. Yu, Y. Zhang, In situ copyrolysis fabrication of $\text{CeO}_2/\text{g-C}_3\text{N}_4$ n-n type heterojunction for synchronously promoting photo-induced oxidation and reduction properties, *J. Mater. Chem. A* 3 (2015) 17120–17130.

[28] X. Li, W. Zhu, X. Lu, S. Zuo, C. Yao, C. Ni, Integrated nanostructures of CeO_2 /at-tapulite/ $\text{g-C}_3\text{N}_4$, as efficient catalyst for photocatalytic desulfurization: mechanism, kinetics and influencing factors, *Chem. Eng. J.* 326 (2017) 87–98.

[29] M. Jourshabani, Z. Shariatinia, A. Baderi, Facile one-pot synthesis of cerium oxide/sulfur-doped graphitic carbon nitride ($\text{g-C}_3\text{N}_4$) as efficient nanophotocatalysts under visible light irradiation, *J. Colloids Interfaces Sci.* 507 (2017) 59–73.

[30] T. Montini, M. Melchionna, M. Monai, P. Fornasiero, Fundamentals and catalytic applications of CeO_2 -based materials, *Chem. Rev.* 116 (2016) 5987–6041.

[31] C. Chang, Y. Fu, M. Hu, C. Wang, G. Shan, L. Zhu, Photodegradation of bisphenol A by highly stable palladium-doped mesoporous graphite carbon nitride ($\text{Pd/mpg-C}_3\text{N}_4$) under simulated solar light irradiation, *Appl. Catal. B: Environ.* 142–143 (2013) 553–560.

[32] D. Gao, Q. Xu, J. Zhang, Z. Yang, M. Si, Z. Yan, D. Xue, Defect-related ferromagnetism in ultrathin metal-free $\text{g-C}_3\text{N}_4$ nanosheets, *Nanoscale* 6 (2014) 2577–2581.

[33] S. Wang, C. Li, T. Wang, P. Zhang, A. Li, J. Gong, Controllable synthesis of nanotube-type graphitic C_3N_4 and their visible-light photocatalytic and fluorescent properties, *J. Mater. Chem. A* 2 (2014) 2885–2890.

[34] X. Liu, Q. Lu, M. Wei, C. Wang, S. Liu, Facile electrospinning of $\text{CeO}_2/\text{Bi}_2\text{WO}_6$ heterostructured nanofibers with excellent visible-light-driven photocatalytic performance, *Chem. Asian J.* 10 (2015) 1710–1716.

[35] T.V.M. Sreekanth, P.C. Nagajyothi, G.R. Dillip, Y.R. Lee, Determination of band alignment in the synergistic catalyst of electronic structure-modified graphitic carbon nitride-integrated ceria quantum-dot heterojunctions for rapid degradation of organic pollutants, *J. Phys. Chem. C* 121 (2017) 25229–25242.

[36] M.E. Khan, M.M. Khan, M.H. Cho, Ce^{3+} -ion, surface oxygen vacancy, and visible light-induced photocatalytic dye degradation and photocapacitive performance of CeO_2 -graphene nanostructures, *Sci. Rep.* 7 (2017) 5928.

[37] R. Rakhmatullin, V. Pavlov, EPR study of nanocrystalline CeO_2 exhibiting ferromagnetism at room temperature, *Phys. Status Solidi B* 3 (2016) 499–503.

[38] S.A. Ansari, M.M. Khan, M.O. Ansari, Band gap engineering of CeO_2 nanostructure using an electrochemically active biofilm for visible light applications, *RSC Adv.* 4 (2014) 16782–16791.

[39] J. Liu, J. Huang, D. Dostosova, Facile synthesis of carbon nitride micro-/nanoclusters with photocatalytic activity for hydrogen evolution, *RSC Adv.* 3 (2013) 22988–22993.

[40] S. Ansari, M.S. Ansari, H. Devnani, $\text{CeO}_2/\text{g-C}_3\text{N}_4$ nanocomposite: a perspective for electrochemical sensing of anti-depressant drug, *Sens. Actuator B-Chem.* 273 (2018) 1226–1236.

[41] K.M. Dunnick, R. Pillai, K.L. Pisane, The effect of cerium oxide nanoparticle valence state on reactive oxygen species and toxicity, *Biol. Trace Elem. Res.* 166 (2015) 96–107.

[42] R. Murugan, G. Ravi, G. Vijayaprasath, Ni- CeO_2 spherical nanostructures for magnetic and electrochemical supercapacitor applications, *Phys. Chem. Chem. Phys.* 19 (2017) 4396–4404.

[43] S. Issarapanacheewin, K. Wetchakun, S. Phanichphant, W. Kangwansupamonkon, N. Wetchakun, Efficient photocatalytic degradation of Rhodamine B by a novel $\text{CeO}_2/\text{Bi}_2\text{WO}_6$, composite film, *Catal. Today* 278 (2016) 280–290.

[44] S. Zhu, S. Liang, Y. Tong, X. An, J. Long, X. Fu, X. Wang, Photocatalytic reduction of CO_2 with H_2O to CH_4 on $\text{Cu}(\text{I})$ supported TiO_2 nanosheets with defective {001} facets, *Mater. Chem. Phys.* 17 (2015) 9761–9770.

[45] W. Xing, C. Liu, Z. Zhou, L. Zhang, J. Zhou, S. Zhuo, Z. Yan, H. Gao, G. Wang, S.Z. Qiao, Superior CO uptake of N-doped activated carbon through hydrogen-bonding interaction, *Energy Environ. Sci.* 5 (2012) 7323–7327.

[46] X. Zou, Z. Wan, C. Wan, G. Zhang, X. Pan, J. Peng, J. Chang, Novel $\text{Ag}/\text{AgCl}/\text{K}_6\text{Nb}_{10.8}\text{O}_{30}$, photocatalyst and its enhanced visible light photocatalytic activities for the degradation of microcystin-LR and acid red G, *J. Mol. Catal. A-Chem.* 411 (2016) 364–371.

[47] Y. Wang, F. Wang, Y. Chen, D. Zhang, B. Li, S. Kang, X. Li, Cui, Enhanced photocatalytic performance of ordered mesoporous Fe-doped CeO_2 , catalysts for the reduction of CO_2 , with H_2O under simulated solar irradiation, *Appl. Catal. B: Environ.* 147 (2014) 602–609.

[48] L. Liu, C. Zhao, Y. Li, Polyaniline-grafted graphene hybrid with amide groups and its use in supercapacitors, *J. Phys. Chem. C* 116 (2012) 7904–7912.

[49] Y. Li, W.N. Wang, Z. Zhan, M.H. Woo, C.Y. Wu, P. Biswas, Photocatalytic reduction of CO_2 , with H_2O on mesoporous silica supported Cu/TiO_2 , catalysts, *Appl. Catal. B: Environ.* 100 (2010) 386–392.